pubs.acs.org/Biomac
Article

Orientation Distribution of Crystalline β-Sheet Domains in *Bombyx mori* Silk Fiber Studied with Vibrational Sum Frequency Generation Spectroscopy

Jihyeong Ryu, Juseok Choi, Jongcheol Lee, and Seong H. Kim*

Cite This: *Biomacromolecules* 2024, 25, 7178−7190
Read Online

ABSTRACT: Silk fibers have good biocompatibility and mechanical properties, which make them attractive in biomaterial applications as well as textile industries. It is believed that the superior mechanical property is associated with the crystalline β-sheet structure in the fiber; but a deeper understanding of the structure−property relationship is still needed for full exploitation of its physical properties. Especially, accurate information on hydrogen-bonding interactions within β-sheet domains at the nanoscale and their spatial distributions at the mesoscale are critically needed. In this study, we demonstrate the selective detection of crystalline β-sheet domains in *Bombyx mori* silk fiber using sum frequency generation (SFG) spectroscopy and its use to determine the angular distribution of the β-sheet crystallites with respect to the fiber axis. Numerical simulations of the SFG signal of the amide-I band were carried out using tensors based on the B2 symmetry of the D_2 point group and compared with experimental data. This comparison found that the crystalline β-sheet domains are aligned along the fiber axis with a standard deviation of ~27° and parallel to the fiber surface with a standard deviation of ~5°. It was also found that the amide bands in the SFG spectra cannot be fully explained with the assumption that the crystalline β-sheet vibrations can be described with the D_2 point group. Being able to monitor the amide group vibrations sensitive to both interchain hydrogen bonding and crystallite orientations, SFG analysis has a potential to unveil the structure−mechanical property relationship that may not be readily assessable with other characterization techniques.

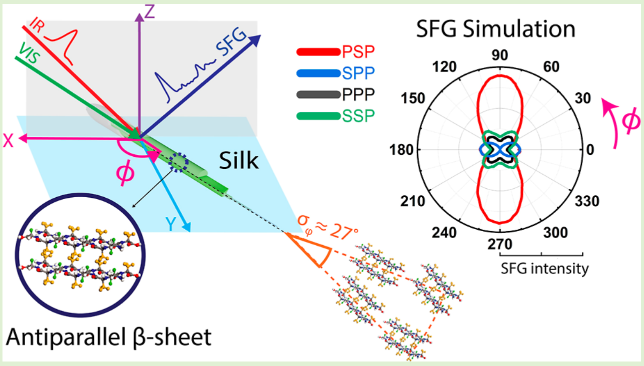

INTRODUCTION

Natural silk fibers, produced by arthropods, notably moths and spiders for sheltering or prey catching, exhibit excellent mechanical properties that engineered polymers cannot match. For example, the dragline of orb-weaver spiders (Araneus) exhibits a high toughness (160 MJ/m^3) with a superior strength (1100 MPa),[1] which surpasses most synthetic fibers, including aramid fibers (such as Kevlar). The good mechanical property is thought to be governed by the crystalline β-sheet domains in the silk.[2,3] If engineers can mimic these properties of natural silk fibers in synthetic fibers, it could enable broader applications in various industrial fields.[4−6] For that, it is needed to better understand the relationship between the crystalline β-sheet structure and the tensile properties of natural silk fibers.[2,7,8]

Although not the toughest, the cocoon fiber of domesticated *Bombyx mori* has been a good model system to study the structure−property relationship of silk because it is readily available.[9,10] The structure of the *B. mori* silk is shown in Figure 1a. At the microscale, each silk thread is comprised of two fibroins, each containing about 1000 bundles of microfibrils, surrounded by sericin layers. Microfibrils are comprised of crystalline β-sheet domains and an amorphous matrix with other secondary structures such as α helices and β turns.[7,11] In general, the crystalline β-sheet domains contain repeating units of glycine (G), L-alanine (A), and L-serine (S); different species spin silk fibers with different amino acid sequences, forming the β-sheet structure. The β sheet of *B. mori* silkworms has a primary motif sequence of $[\mathrm{GAGAGS}]_n$.[12,13] Due to the shear during the fiber spinning, individual β strands are aligned along with the fiber direction.[2,8,14] Through hydrogen-bonding interactions between C═O and H−N groups in adjacent β strands, they can form antiparallel-packed pleated sheets. The stacking of the hydrophobic facets of these sheets through van der Waals interactions leads to a crystalline β-sheet domain.[12,15] In the crystalline unit cell, the C═O···H−N

Received: June 6, 2024
Revised: October 2, 2024
Accepted: October 3, 2024
Published: October 16, 2024

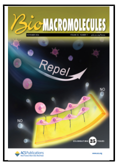

ACS Publications

https://doi.org/10.1021/acs.biomac.4c00774

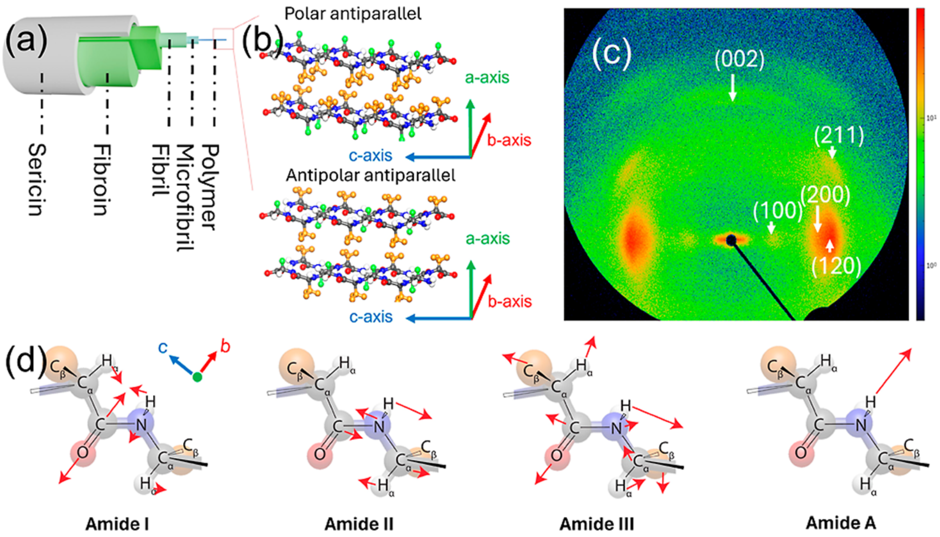

Figure 1. (a) Hierarchical structure of *B. mori* silk fiber containing antiparallel β-sheet domains. (b) Schematic illustration of two possible stacking patterns of β sheets. (c) 2D-XRD pattern of *B. mori* fibers aligned along the meridional direction. (d) Normal modes of amide bands; C_α, C_β, and H_α represent the carbon center of amino acid, the side group carbon, and hydrogen bonded to the carbon center, respectively.

hydrogen bonds are along the *b* axis and the hydrophobic stacking is along the *a* axis.

The crystalline β-sheet domain structure has been characterized extensively with X-ray diffraction (XRD), nuclear magnetic resonance (NMR), and infrared (IR) and Raman spectroscopy. In 1955, Marsh et al. conducted XRD analysis and proposed a polar antiparallel structure, in which the methyl groups of alanine in β strands in one sheet are pointing in the same direction and these directions vary alternatively among adjacent sheets (see the top image in Figure 1b).[16] In 1979, Lotz and Cesari proposed an alternative structure which contained less-regularly aligned strands.[17] Based on further XRD analysis, Takahashi et al. suggested that an antipolar antiparallel packing model is more suitable than polar antiparallel packing; in the antipolar packing, the methyl groups between adjacent β strands in one sheet point in opposite directions (see the bottom image in Figure 1b).[15] Later, an NMR study also supported the antipolar antiparallel model.[18] Since the shear action during the fiber spinning aligns the β strands along the fiber direction, the (002) diffraction peak of the crystalline β sheet appears in the meridional direction and the (*hk*0) peaks are in the equatorial direction in 2D-XRD of silk fiber (Figure 1c).[19]

Although XRD can provide crystallographic dimensions and orientations, it cannot provide subtle changes in hydrogen-bonding interactions because the X-ray scattering cross section of hydrogen is essentially zero. Additionally, XRD suffers from diffuse scattering signals from the amorphous matrix, especially when the crystallinity is low and crystals are small in size.[20,21] NMR can provide additional structural information such as dihedral angles of amide bonds, but it cannot provide information on crystallite distributions in space.[18,22]

Vibrational spectroscopy has been extensively used for qualitative and quantitative analysis for secondary structures of proteins that are sensitive to interchain hydrogen-bonding interactions.[23] Figure 1d illustrates the characteristic normal modes of peptide backbone vibrations widely used in vibrational spectroscopy. The amide-I modes in the 1600−1700 cm^{-1} region are predominantly C═O stretching with minor contributions from CN stretching and NCC deformation of the peptide backbone.[23,24] The contribution from the side groups attached to the C_α position is considered to be negligible in the amide-I mode. For that reason, the amide-I band can be deconvoluted with characteristic modes of different secondary structures of the peptide chains, regardless of the identity of the side groups.[23−25] Although the vibrational modes in the amide-II and -III bands are coupled with side groups, their peak positions can also be related to specific secondary structures of proteins. The amide-II modes in the 1500−1580 cm^{-1} region involve NH in-plane bending and CN stretching, with some contributions from H_α bending.[23,24] The amide-III modes in the 1200−1300 cm^{-1} region involve coupling of various modes including NH in-plane bending, CN stretching, H_α bending, and vibrations of other side groups at the C_α position.[24,26] The amide-A band at ∼3300 cm^{-1} and the amide-B band at 3050 cm^{-1} are the Fermi resonance doublets of the NH stretching mode and the overtone of the amide-II mode.[24]

Although these assignments show the potential of using vibrational spectroscopy to study hydrogen-bonding interactions and conformational changes in the crystalline β-sheet domains in the silk fiber, the practical usage of conventional IR and Raman analysis methods suffers from uncertainties in peak deconvolution especially when the crystallinity of the sample is low. For example, the IR peaks in the amide-I band region of silk could be deconvoluted with multiple peaks (in some cases, up to ten components), which are highly subjected to the choice of spectral parameters used for peak fitting. Thus, fitting results may vary drastically depending on constraints in full width half-maximum (fwhm), peak position, etc.[27−29] In the case of quantification of crystalline β-sheet domains in silk, it is often difficult to reliably and accurately distinguish and subtract the amorphous contributions from the experimental spectrum.

The complexity associated with signals from the amorphous phase can be completely avoided in nonlinear spectroscopy, such as vibrational sum frequency generation (SFG) spectroscopy. Being a nonlinear optical process, SFG requires noncentrosymmetry;[30−33] this means that amorphous (random) phases cannot produce the SFG signal and only

https://doi.org/10.1021/acs.biomac.4c00774
Biomacromolecules 2024, 25, 7178−7190

crystalline domains without centrosymmetry can be detected selectively in SFG.[30−33] This has been demonstrated in structural analysis of various crystalline biopolymers including cellulose, chitin, amylose, collagen, and so on.[31−34] The SFG signal intensity is proportional to the square of the nonlinear second-order susceptibility ($\chi_{ijk}^{(2)}$) which can be described as[31−36]

$$\chi_{ijk}^{(2)} \propto N \sum_{i',j',k'} \langle R_{ii'} R_{jj'} R_{kk'} \beta_{i',j',k'} \rangle \quad (1)$$

where N is the number density of SFG-active domains within the SFG coherence length, $\beta_{i',j',k'}$ is the molecular hyperpolarizability of the SFG-active vibrational mode, and $R_{ii'}R_{jj'}R_{kk'}$ is the Euler transformation matrix projecting the i',j',k' molecular coordinate (a,b,c) to the i,j,k lab coordinate (X,Y,Z) using three polar coordinate angles, namely, tilt (θ), azimuth (ϕ), and twist (ψ) angles (see Figure S1 for the angular representation). Thus, if the hyperpolarizability ($\beta_{i',j',k'}$) of the vibrational mode of interest is known, the SFG signal intensity can be calculated theoretically with proper angular distributions of SFG-active vibrational modes.[35,37,38]

In this study, we demonstrate the selective detection of the crystalline β-sheet domain in *B. mori* silk fiber with SFG, discuss the assignment of the vibrational peaks detected with SFG, and determine the orientational distribution of β-sheet domains in *B. mori* silk fiber. The SFG spectra with amide bands are compared with the polarized IR and Raman spectra. The $\beta_{i',j',k'}$ term has a nonzero value only when the vibrational mode is both IR- and Raman-active.[35,37,38] For that reason, the comparison of SFG spectral features with the IR and Raman spectra can facilitate the peak identification and interpretation.[30,31] In the previous SFG study of model proteins, it was suggested that the SFG signal of the amide-I band could be modeled with the B2 symmetry of the D_2 point group.[38,39] We used this symmetry-based $\beta_{i',j',k'}$ argument for the amide-I band and carried out theoretical predictions of the azimuth angle dependence of the SFG signals at four SFG polarization combinations for various tilt and azimuth angles. By comparing the theoretically calculated SFG intensity ratios with the experimental data, it was possible to determine the angular orientation distribution of the crystalline β sheets in the *B. mori* silk fiber. From this study, we also found the limitation of the point group symmetry-based approach, which invites further development of the $\beta_{i',j',k'}$ calculation. Nonetheless, it is still possible to assess the potential to use SFG characterization to unveil the structure−property relationship of silk fibers.

■ EXPERIMENTAL SECTION

Materials. Silk fibroin powder (product no. 925802) was obtained from Sigma-Aldrich, and methanol (product no. BDH2018-1GLP) was purchased from VWR International. Degummed *B. mori* silk fibers were purchased from Living Dreams Yarn Co. All materials were used as received.

Preparation of Samples. Fibroin powders were pelletized into disks (7 mm diameter, 1 mm thick) using a minipellet press (Specac, UK). These fibroin pellets were immersed in 30 mL of methanol to recrystallize β-sheet structures. After a designated treatment time, each pellet was retrieved from the methanol solution and residual methanol was wiped off using a dust-free tissue. The pellets were then dried under vacuum for 2 days at room temperature. Detailed experimental procedures can be found elsewhere.[28,40] Since particles in the fibroin pellet had no specific order or orientation, they were directly placed on the sample stage without any specific orientational mark. The silk fiber samples were used as received without additional chemical treatment. The fiber samples were combed for uniform alignment, and the top and bottom regions were affixed to a substrate (slide glass) using ultraviolet resin.

X-ray Diffraction. Two-dimensional (2D) XRD in transmission mode was performed using a Xeuss 2.0 HR (Xenocs, France) with a copper (Cu) X-ray wavelength of 1.54 Å (50 kV, 0.6 mA) and a Dectris Pilatus3 R 200 K detector.

Attenuated Total Reflection IR and Raman Spectroscopy. Fourier-transform IR (FT-IR) spectroscopy measurements were conducted using a Bruker Vertex 80 spectrometer (Bruker Optics) with a mercury−cadmium−telluride (MCT) detector. Diamond and ZnSe crystals were used for attenuated total reflection (ATR)-IR and polarized IR, respectively. The FT-IR spectra of fibroin and silk samples were analyzed from 400 to 4000 cm^{-1} with 400 scans. The polarized Raman analysis was performed using LabRAM HR (Horiba) with a 644 nm excitation laser source and 300 gr/nm grating.

SFG Spectroscopy. Broad-band SFG (BB-SFG) experiments were conducted using 800 nm wavelength pulses (laser width ∼85 fs, 2 kHz repetition rate) from a Ti/sapphire femtosecond laser system. The bandwidth of IR was in the range of 150−200 cm^{-1}, depending on the energy range. A detailed description of the SFG system can be found elsewhere.[41] The 800 nm (denoted as Visible for convenience) and mid-IR incident lasers were focused on the silk fiber sample through a BaF_2 lens (focal point, f = 15 cm) at an incidence angle of 45° from the surface normal direction. A small fraction of SFG signals emitted with a wide distribution of solid angles (Figure S1) was collimated and directed to a spectrometer equipped with a volume-phase holographic grating (Andor, HoloSpec) and a CCD camera (Andor, DU420A-BEX2-DD). Two separate gratings were used for the low wavenumber (1100−2000 cm^{-1}) and high (2500−4000 cm^{-1}) regions. In this study, the coherence length of SFG was about 250 nm (based on the incident angles and dispersion of refractive index), and the diameter of the irradiated area was ∼5 μm, respectively. Note that this coherence length is not the probe depth from the external surface of the silk fiber. Since the scattered signal from the bulk phase was detected, the probe depth was mostly governed by the IR attenuation length in the sample. The coherence length was just a rough estimate of the length scale within which SFG signals from different domains will interact with each other. This estimation was needed to run the numerical simulations. The SFG spectra were collected for fiber samples set to azimuth angles (ϕ) of 0, 45, and 90°. The multiple spots were analyzed with BB-SFG with a mid-IR range of 1000−1800 cm^{-1} and 2700−3800 cm^{-1} with intervals of 100 cm^{-1} for low and high wavenumber regions, respectively. To average the SFG spectra, each spectrum was normalized by the highest peak (i.e., 1262 and 3275 cm^{-1} for low and high wavenumber region, respectively). In this way, the spectral shape of each spectrum was maintained. At each azimuth angle, the spectra were collected at at least three spots per fiber and then averaged. The expression of the SFG polarization combination follows the three-letter convention, with each letter (s or p) describing polarizations in the order of SFG-VIS-IR beams. For example, the psp polarization indicates that SFG polarization is p, 800 nm polarization is *s*, and IR polarization is p with respect to the laser incidence plane. The SFG spectra were collected with psp, spp, ssp, and ppp polarizations. The other four polarizations (sps, spp, pps, and sss) were not used, since the psp, spp, ssp, and ppp polarizations gave a sufficient data set to determine the orientation information on the crystalline β sheet with respect to the fiber axis.

Numerical Simulation of SFG. Numerical simulations were performed using Mathematica software; the detailed methods for numerical SFG simulation are described elsewhere.[35] The simulation variables included azimuth angle (ϕ), tilt angle (θ), twist angle (ψ), standard deviation of the β-sheet alignment along the fiber axis (σ_φ), and standard deviation of the tilt angle of the β sheet inside the fiber (σ_θ). VIS and IR incident angles were set at 45°, the refractive index of *B. mori* silk was 1.55,[42,43] and the refractive index at the interface

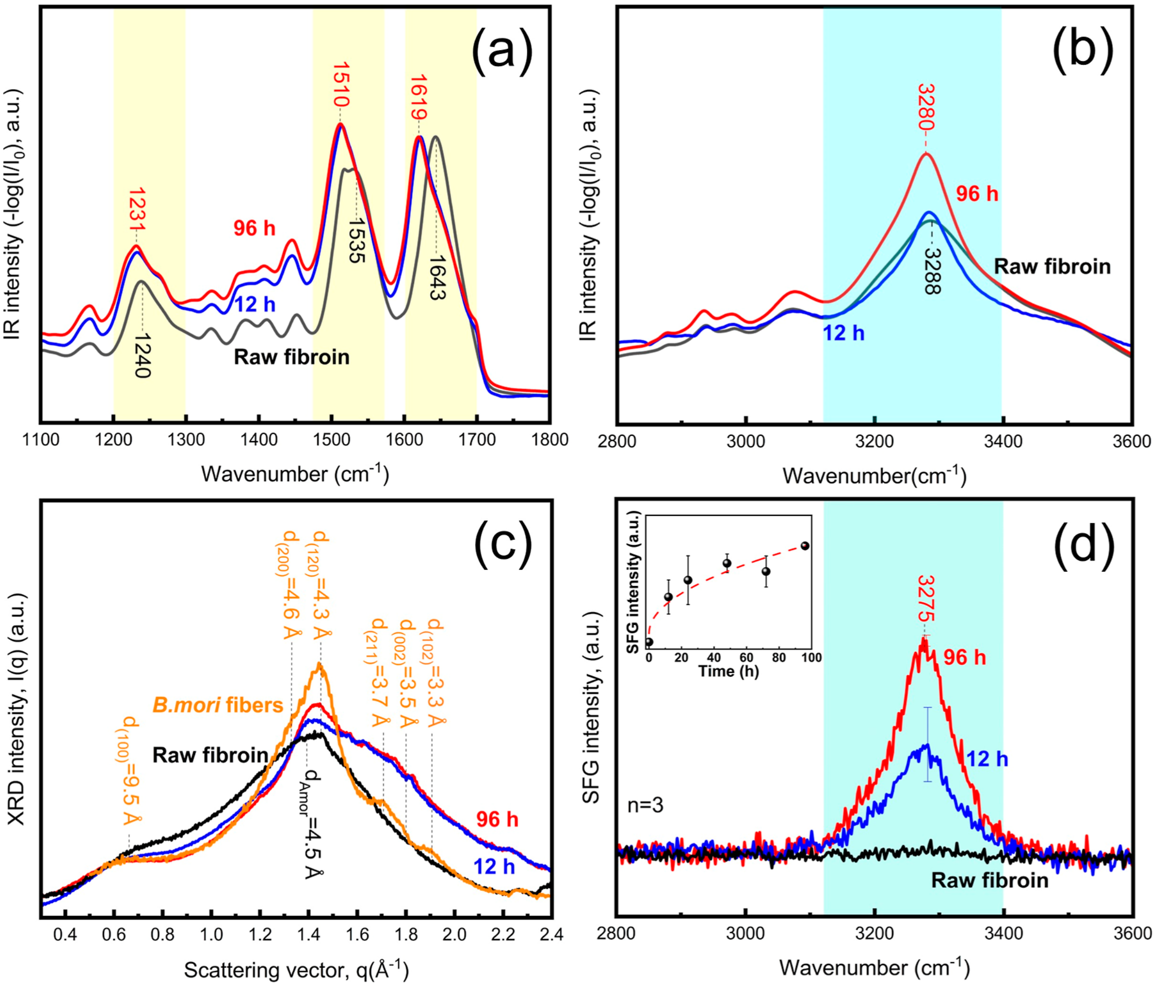

Figure 2. (a,b) ATR-IR spectra, (c) XRD patterns, and (d) ssp-SFG spectra analysis of recrystallized fibroin before and after methanol treatment. In (a,b), peak intensities were normalized by the intensity of a maximum peak of 1510 cm^{-1}. In (c), diffractograms were normalized at q = 0.6 Å^{-1}. In (c), the diffraction peaks of the crystalline β-sheet structure in *B. mori* fiber are marked with the corresponding Miller indices and d spacing. The inset in (d) shows the methanol treatment time (x axis) versus SFG intensity (y axis).

was set with the value of 1.20.[36] The IR transition dipole moment and Raman polarizability tensors of the antiparallel β sheet were calculated following the methods described in the previous literature.[38,39] The z-y-z Euler transformation was used for given tensors to transform the tensors in the molecular frame to the laboratory coordinates. The tensors for four possible amide-I modes of the antiparallel β sheet were calculated for the peptide bond with the D$_2$ point group. Azimuth angle polar plots for four polarization combinations were obtained by creating 1000 replicas with Gaussian distribution probabilities with angle distributions (σ_φ and σ_θ) at every 1.5° increment and then taking an azimuth average of 1000 cases at each azimuth angle.

RESULTS AND DISCUSSION

Selective Detection of the Crystalline β Sheet by SFG.

Figure 2 demonstrates the capability of SFG to selectively detect the crystalline β-sheet fraction in silk. It compares the IR spectra, XRD patterns, and SFG spectra of raw amorphous fibroin and methanol-treated fibroin. The methanol treatment is known to induce crystalline β-sheet folding;[28,40] so, it was used as a control experiment. Upon methanol treatment, the amide-I band in IR shifts from 1643 to 1619 cm^{-1} and the amide-II band moves from 1535 to 1510 cm^{-1} (Figure 2a). In the amide-III band region, the peak at 1240 cm^{-1} splits into two peaks at 1231 and 1262 cm^{-1} as the crystalline β-sheet structure is induced through the methanol treatment. The amide-A band exhibits a small red shift from 3288 to 3280 cm^{-1} and becomes narrower (Figure 2b). The decrease in the N−H stretch band position means a stronger hydrogen-bonding interaction,[44,45] and the narrowing of fwhm indicate that the hydrogen-bonding distribution becomes more uniform as amorphous peptide chains are ordered into the crystalline β-sheet structure. These spectral changes confirm the recrystallization of the β-sheet structure in the methanol-treated fibroin sample.[28,46,47]

XRD also confirms the formation of crystalline β-sheet domains upon methanol treatment (Figure 2c). The raw fibroin shows a very broad amorphous scattering background centered at $q \approx 1.5$ Å^{-1}. The recrystallized samples exhibit the growth of intensity at q positions corresponding to the (100) and (120) planes of the β-sheet crystallites, indicating crystalline order along the hydrogen-bonding axis and stacking of the β-sheet structure, respectively. Although not definitive, the growth of other diffraction peaks corresponding to the (211), (002), and (102) planes is noticeable.[8,48,49] The 1D-XRD spectra derived from the intensity profile along the equator and meridian of the 2D-XRD of *B. mori* silk fibers (shown in Figure 1c) are shown in Figure S2, along with the d-spacing and crystal size calculation results in Table S1 for

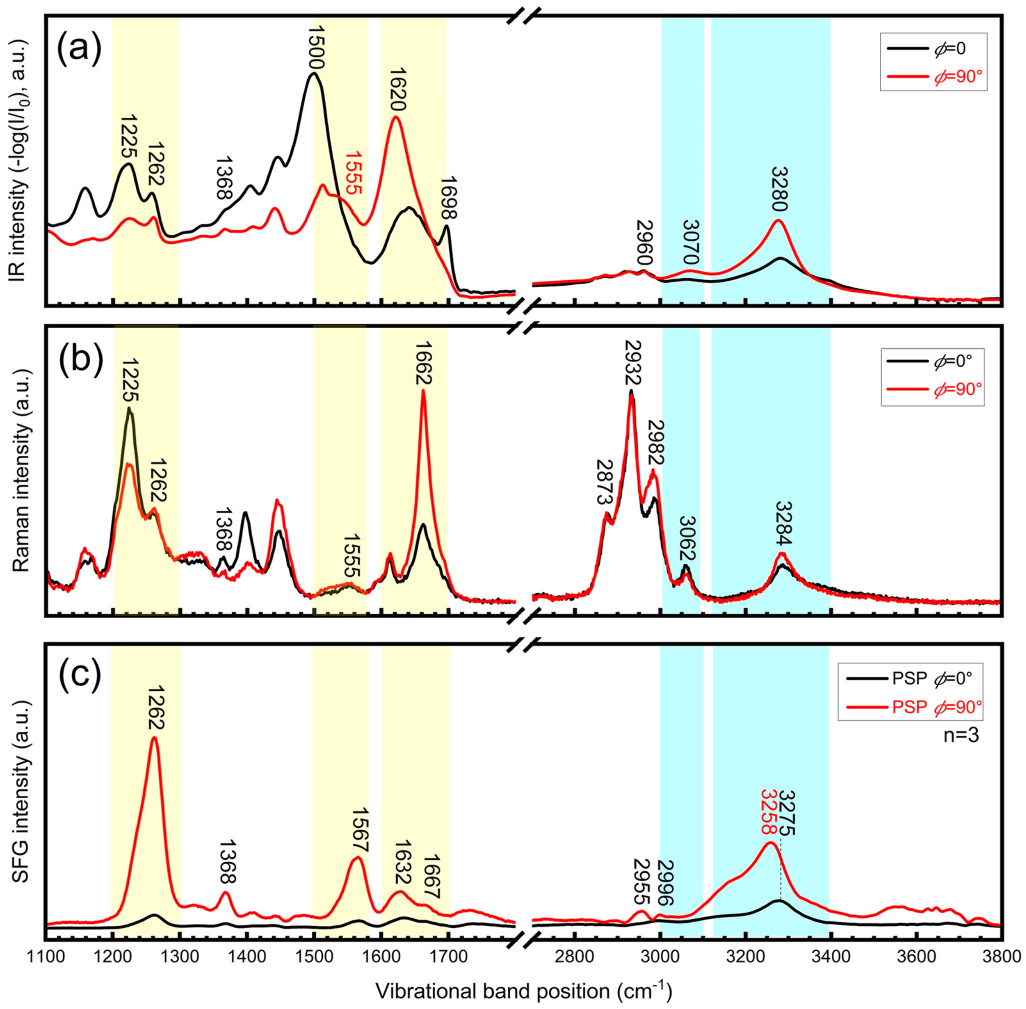

Figure 3. (a) Polarized ATR-IR spectra, (b) polarized Raman spectra, and (c) psp-SFG spectra of *B. mori* silk fibers at the polarization axis or incident plane parallel ($\phi = 0^\circ$) and perpendicular ($\phi = 90^\circ$) to the fiber axis. Peaks at 2925 and 2932 cm^{-1} were chosen for normalization for IR and Raman, respectively. SFG spectra have ratioed by a 1:3.5 ratio for the parallel and perpendicular azimuth angle based on the simulation result with angular distributions σ_φ, σ_θ=(27.5, 5°).

comparison. The 2D-XRD image of the recrystallized β-sheet structure displays a halo, indicating that there is no preferential ordering of the crystalline domains (Figure S3).

Figure 2d shows the growth of the SFG signal from the fibroin pellet with methanol treatment time. The raw fibroin did not show any SFG signal in the amide-A band region because it was totally amorphous. As the degree of recrystallization increases, the SFG signal of the amide-A band of the crystalline β sheet at 3275 cm^{-1} also increases. Note that the surface-SFG signal can also be generated,[50] but its contribution is negligible compared to the bulk-SFG signal.[51] The SFG signal intensity grew with the $\sqrt{t}$ dependence, which may indicate that the recrystallization kinetics is governed by the diffusion of methanol into the fibroin pellet.[52,53]

Comparison of IR, Raman, and SFG Spectra of *B. mori* Silk. Figure 3 compares the polarized-IR, polarized-Raman, and psp-SFG spectra of the *B. mori* silk fiber. Here, we are comparing the psp-SFG spectra since this polarization gave the strongest signal; the full polarization comparison is shown in Figure 4. Table 1 summarizes the positions of the peaks identified in IR, Raman, and psp-SFG spectra and their assignments based on the literature and the SFG principle. Since the SFG-active peaks should be both IR- and Raman-active, the absence of certain peaks in SFG can be explained by that requirement. For example, the 1662 cm^{-1} mode is known to be Raman-active but IR-inactive;[38,56] thus, there is no noticeable peak at 1662 cm^{-1} in the SFG spectra. The amide-II peak at 1500−1520 cm^{-1} is IR-active but Raman-inactive;[14,57] thus, there is no peak in that region in the SFG spectra.

The relative peak intensities in the SFG spectra are quite different from those in the IR and Raman spectra.[25,31,58] For example, although the ∼1550 cm^{-1} peak in the amide-II band region is weak in both IR and Raman spectra, it is very strong in the SFG spectra. In the amide-III band region, the 1223−1225 cm^{-1} peak is strong in both IR and Raman spectra but negligible in the SFG spectra; in contrast, the 1260 cm^{-1} peak is weaker in both IR and Raman spectra but very strong in the SFG spectra. The amide-I band shape resembles the IR band but is quite different from the Raman band in the same spectrum region. The CH stretch vibrations are very strong in Raman; although weak, they can be seen clearly in IR. In SFG, the CH stretch peak intensities are extremely small (almost negligible) compared with the amide-A band. The amide-B band is noticeably absent in both IR and Raman spectra, but it is completely missing in the SFG spectra.

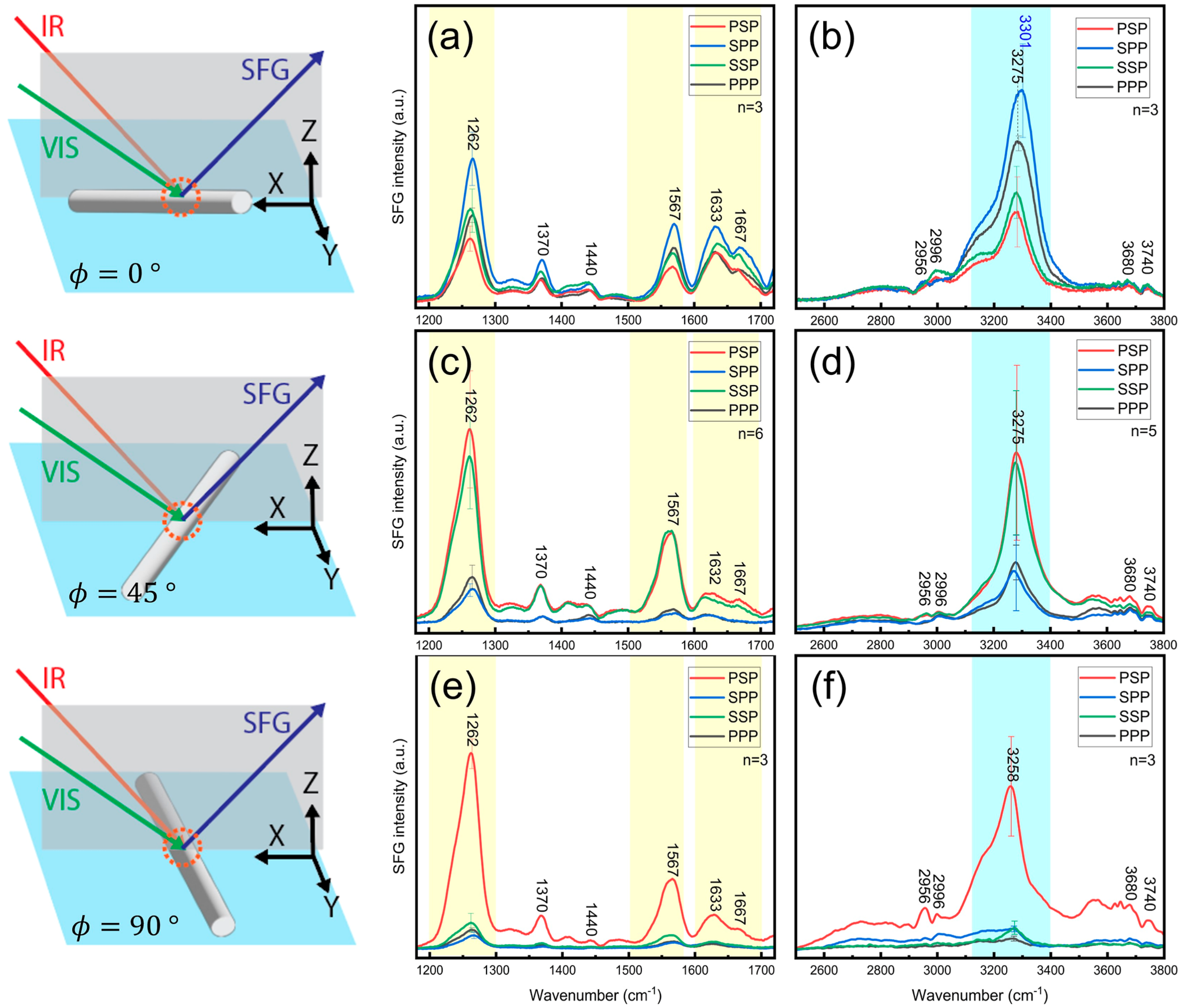

Figure 4. SFG spectra of degummed *B. mori* fibers for (a,c,e) low and (b,d,f) high wavenumber regions at (a,b) $\phi = 0°$, (c,d) $\phi = 45°$, and (e,f) $\phi = 90°$.

If we look at the peptide bond units only in the antiparallel β-sheet structure, they belong to the D_2 point group.[38,59] The unit cell of the antiparallel β-sheet structure has four peptide groups: two in one chain (along the *c* axis) and two in the adjacent chain (along the *b* axis). In the D_2 point group, four symmetry-allowed normal modes are A(0,0), B1(0,π), B2(π,0), and B3(π,π).[24,38,56] The character table of the D_2 point group is shown in Table 2. In the parentheses, the first number is the intrachain phase difference of the IR-transition dipoles of two groups in each chain and the second is the interchain phase difference between two adjacent chains.[24,38,56] The amide-I band of the antiparallel β sheet is split into 1632 and 1698 cm^{-1}.[14,24,56] The former has B2 symmetry; the latter can be assigned to B1 symmetry since it has a relatively strong intensity in the IR with polarization parallel to the *c* axis (Figure 3a). In the D_2 point group character table, the B2 mode is both IR- and Raman-active; thus, the 1632 cm^{-1} peak appears in SFG. The transition dipole moment of the B2 mode is along the *b* axis (i.e., perpendicular to the *c* axis).[23,24] The B1 mode is also both IR- and Raman-active; its transition dipole moment is along the *c* axis. Nonetheless, the SFG spectra in Figure 3c do not show a noticeable peak at 1698 cm^{-1}. The absence of this peak is explained in the next section. The strong peak at 1662 cm^{-1} in the Raman spectra has the A symmetry in the D_2 point group, which is Raman-active but IR-inactive; thus, this peak is not observed in SFG. We can see a small SFG peak at ~1667 cm^{-1}; based on its intensity relative to the 1632 cm^{-1} intensity, we can tentatively attribute it to the B3 mode (which is explained in the next section). The transition dipole moment of the B3 mode has a small component perpendicular to the *c* axis (along the *a* axis of the unit cell).[23]

In the previous SFG analysis of model peptides with short amino acid sequences, the amide-III band has not attracted much attention. One reason is that it was not expected to be detected in SFG because the amide-III mode is thought to have B1 symmetry in the D_2 point group (same as the 1698 cm^{-1} mode). Also, because it is coupled with deformations of the side groups at the C_α position, its interpretation is somewhat complicated. Nonetheless, the psp-SFG spectra of *B.*

Table 1. Vibrational Modes of Peaks Detected in the IR, Raman, and SFG Spectra of *B. mori* Fiber

band	IR [cm^{-1}]	Raman [cm^{-1}]	SFG [cm^{-1}]	force-field[24] calculation for poly(GA), β sheet[a]	assignment	symmetry in D_2 point group
amide A	3275	3289	3275	NH str	β sheet[47]	
amide B	3070	3063		Fermi resonance of NH str and amide-IIovertone	β sheet[47]	
CH str	2980	2990	2996	CH_3 asym str		
			2946			
		2871	2873	$C_\alpha H_\alpha$ str		
amide I	1698(//)	(weak)		C═O str (76), CN str (15), C_αCN def (12)	β sheet[14,28,54]	B1(0,π)
	1690−1660	1690−1660			β turns[14,27,28]	
	NR	NR	~1667		β sheet (TA, this work)	B3(π,π) +
	NA	1662(⊥)		C═O str (76), CN str (15), CCN def (12)	β sheet[27]	A (0,0)
	1645−1650				α helix[14,28] (amorphous)	
	1630(⊥)	(weak)	1632(⊥)	C═O str (77), CN str (14), CCN def (12)	β sheet[28,38,47]	B2(π,0)
	1615	1613	1616		aggregated β strands[55]	
amide II	1555(⊥)	1555	1567	NH ipb (41), CN str (24), C_αC str (15), NC_α str (11)	β sheet (IR,⊥)[14]	
			1555			
	1535				amorphous[14]	
	1507−1518(//)	NA			β sheet[14]	
CH def	1447	1447 (1440)[a]	1440	CH_2 bend	CH_α bending[11]	
	1371	1369	1370	CH_3 sym bend (25)	CH_3 of alanine in the β sheet[11]	
				H_α bend (17), NH ipb (12), CH_2 wag (10)		
	1327	1334		CH_3 sym bend (62), H_α bend (22)	CH_3 of alanine in the β sheet[11]	
amide III	1262	1262	1262	NH ipb (32), C═O ipb (15), COC str (15)	β sheet[46]	
	1225	1223	(weak)	CH, twist (23), NH ipb (18), CH, wag (16), H_α bend (15), CN str (14)	β sheet[11]	

[a] (sym = symmetric, asym = asymmetric, str = stretching, def = deformation, ipb = in-plane bending, wag = wagging, NA = not active, NR = not resolved, + = tentatively assigned, numbers in parenthesis indicate vibrational contributions).

Table 2. Normal Mode Symmetry in the D_2 Point Group of the Antiparallel β Sheet[a]

symmetry	$\left(\frac{\partial \alpha_{i'j'}}{\partial Q_q}\right)$	$\left(\frac{\partial \mu_{k'}}{\partial Q_q}\right)$	peak within the amide-I region (cm^{-1})
A symmetry, υ(0,0)	$\begin{pmatrix} 1.018 & 0 & 0 \\ 0 & 7.709 & 0 \\ 0 & 0 & 2.172 \end{pmatrix}$	$\begin{pmatrix} 0 \\ 0 \\ 0 \end{pmatrix}$	1662
B1 symmetry, υ(0,π)	$\begin{pmatrix} 0 & 1.220 & 0 \\ 1.220 & 0 & 0 \\ 0 & 0 & 0 \end{pmatrix}$	$\begin{pmatrix} 0 \\ 0 \\ -0.032 \end{pmatrix}$	1698
B2 symmetry, υ(π,0)	$\begin{pmatrix} 0 & 0 & -1 \\ 0 & 0 & 0 \\ -1 & 0 & 0 \end{pmatrix}$	$\begin{pmatrix} 0 \\ 1 \\ 0 \end{pmatrix}$	1632
B3 symmetry, υ(π,π)	$\begin{pmatrix} 0 & 0 & 0 \\ 0 & 0 & -2.115 \\ 0 & -2.115 & 0 \end{pmatrix}$	$\begin{pmatrix} 0.168 \\ 0 \\ 0 \end{pmatrix}$	1667

[a] The tensor components are normalized with the values in the B2 symmetry.

mori silk show a very strong peak at 1262 cm^{-1}, even stronger than the amide-I mode. This suggests that coupling with the side group deformation breaks the B1 symmetry and makes the 1262 cm^{-1} mode SFG-active. At this moment, it is not explained why the 1225 cm^{-1} peak is negligible in the SFG spectra of *B. mori* silk, while the 1265 cm^{-1} peak is strong.

In any case, these comparisons show that the full interpretation of the SFG spectra of the crystalline β sheet inside the *B. mori* silk is a lot more complicated than the previous SFG analysis of protein moieties which was done for the 2D interfaces with C_∞ symmetry.[38,39,60] For full interpretation of the SFG spectral features of crystalline β sheets in silk fibers,[24,61] a full set of $\beta_{i',j',k'}$ tensor components are required, which is beyond the scope of the current experimental study.

Polarization and Azimuth Angle Dependence of SFG Spectral Features of the β Sheet in *B. mori* Silk. If the SFG-active domains are distributed in an amorphous matrix without any specific orientations (i.e., completely random), then there will be no polarization and/or azimuth angle dependence of SFG spectral features.[30,35] But, from the 2D-XRD pattern shown in Figure 1c, we know that the crystalline β-sheet domains are preferentially aligned along the fiber axis. Thus, the SFG spectral features will have the polarization and azimuth angle dependences. Figure 4 plots the psp, spp, ssp, and ppp SFG spectra collected at azimuth angles of 0°, 45°, and 90°. Note that when the silk fiber was rotated to measure SFG spectra at different azimuth angles, different locations of the fibers were measured. Moreover, the incident angle of the beam with respect to the tangential plane of the rounded fiber surface was also changed upon rotation of the sample. So, the absolute intensity cannot be compared among the spectra collected at different azimuth angles. Moreover, different gratings were used in the monochromator for the low and high wavenumber regions; so, the relative intensities of the amide-I, -II, and -III modes versus the amide-A mode cannot be compared. Nonetheless, the relative intensities of the spectra collected with different polarizations at a given azimuth angle within each spectral region can still be compared since they were collected without moving the sample; just the polarizations of the 800 nm incoming beam and the SFG signal were rotated. In our system, changing the IR polarization inevitably caused displacement of the beam spot position; for that reason, we did not change the IR polarization.

In general, the polarization dependences of all vibrational peaks show similar patterns. At 0° of the azimuth angle between the fiber and the laser incidence plane (i.e., $\phi = 0°$), the intensities of all peaks are slightly larger in the spp polarization than the other three cases, i.e., $I_{spp} > I_{ppp} \approx I_{ssp} \approx I_{psp}$ in the amide-I, -II, and -III band regions (Figure 4a). The amide-A peak shows a somewhat different pattern: $I_{spp} > I_{ppp} > I_{ssp} \approx I_{psp}$ (Figure 4b). At $\phi = 45°$, we see $I_{psp} \approx I_{ssp} \gg I_{spp} \approx I_{ppp}$ in both high and low wavenumber regions (Figure 4c,d). At $\phi = 90°$, the relative intensity pattern is $I_{psp} \gg I_{spp} \approx I_{ssp} \approx I_{psp}$ in both high and low wavenumber regions (Figure 4e,f). Each SFG spectrum in the low wavenumber region was fitted with 13 components (including 3 components in the amide-I region, 2 in amide-II, and 3 in amide-III) and the fit results are shown in the Supporting Information (Figures S4−S6).

The amide-A band shows a slight shift in the peak position with ϕ; 3300 cm^{-1} in ppp but 3275 cm^{-1} in psp, spp and ssp at $\phi = 0°$, 3275 cm^{-1} in all polarizations at $\phi = 45°$, and 3258 cm^{-1} in all polarizations at $\phi = 90°$. All other peaks do not exhibit any noticeable shift in the peak position with ϕ. At this moment, we cannot interpret the physical meaning of these slight shifts in the amide-A peak position at different polarizations and azimuth angles. Since the α helices and random coils in the amorphous fibroin did not show any detectable SFG signals in the amide-A region (Figure 2), this SFG signal must come solely from the crystalline β sheet. The shift in the peak position with the probe beam polarization and azimuth angle could mean the presence of multiple modes with slightly different hydrogen-bonding interactions and orientations within the β-sheet structure of the *B. mori* silk fiber. Further analysis could not be done without knowing the full $\beta_{i'j'k'}$ tensors.

The relative intensities between the 1567 cm^{-1} peak (amide-II) and the 1262 cm^{-1} peak (amide-III) do not change drastically with the azimuth angle change; but the relative intensity of the amide-I band at 1632 cm^{-1} with respect to these two bands is changing significantly: $I_{1632} \approx I_{1567}$ at $\phi = 0°$, but $I_{1632} < I_{1567}$ at $\phi = 45$ and 90°. Thus, the polarization and azimuth angle dependences of the 1632 cm^{-1} peak can be analyzed further in terms of the orientation distribution of the crystalline β sheet in the *B. mori* silk fiber.

Orientation Distribution Analysis Based on the Amide-I Band of the Antiparallel β Sheet in *B. mori* Silk. As mentioned in Table 1, the amide-I groups in the antiparallel β-sheet structure could be analyzed with the symmetry argument within the D_2 point group.[38,56] Using the Raman polarizability and IR transition dipole orientation of the O═C−N stretch modes and their atomic coordination,[38] the Raman polarizability derivative and IR transition dipole derivative tensors, i.e., $\left(\frac{\partial \alpha_{i'j'}}{\partial Q_q}\right)$ and $\left(\frac{\partial \mu_{k'}}{\partial Q_q}\right)$, can be calculated for the amide-I mode of the antiparallel β sheet, from which the hyperpolarizability tensor could be calculated. In the literature, two calculation methods are available.[38,39] Both used the same approach, but due to a slight difference in atomic coordinates, the values are slightly different. The values proposed by Nguyen et al. are shown in Table 2,[38] and the values proposed by Ye et al. are shown in Table S5 in the Supporting Information for comparison. Then, the hyperpolarizability of the amide-I mode can be expressed as the tensor product of these two

$$\beta_{i'j'k'} \propto \left(\frac{\partial \alpha_{i'j'}}{\partial Q_q}\right) \otimes \left(\frac{\partial \mu_{k'}}{\partial Q_q}\right) \tag{2}$$

The normal mode with A symmetry has $\left(\frac{\partial \mu_{k'}}{\partial Q_q}\right) = 0$; thus, $\beta_{i'j'k'}$ is always zero. This explains the absence of 1662 cm^{-1} in the SFG spectra. The normal modes with B1, B2, and B3 symmetries, in principle, can be SFG-active because they have nonzero $\beta_{i'j'k'}$ components. In order to predict the SFG intensity using eq 1, we multiply the Euler transform matrix to each $\beta_{i'j'k'}$ and then integrate all terms with proper normalization factors to get $\chi^{(2)}_{ijk}$. Since the (002) diffraction peak of the β sheet is along the fiber direction in the 2D-XRD (Figure 1c), we assumed that the peptide chain axis is aligned along the fiber axis [i.e., the alignment angle (φ) between the *c* axis of the β-sheet crystal and the fiber axis is zero]. Since the IR beam is attenuated as it travels inside the fiber and the transmittance of the probe beams at the air/fiber interface is largest at the top surface of the fiber and negligible at the side surface of the fiber, we assumed that the β-sheet crystallites near the top surface of the silk fiber would give the largest contribution to the SFG signal. For that reason, we set the average value of the tilt angle of the β sheet with respect to the XY plane to be zero ($\theta = 00°$, with respect to the Z axis). We also assumed that there is no preferential rotational angle of the crystalline domain along the peptide chain axis; thus, the twist angle term was integrated over 360° with equal probability. Then, we obtain the effective susceptibility, $\chi^{(2)}_{\text{eff}}$, as a function of the azimuth angle (ϕ) of the fiber with respect to the lab coordinate. For the normal mode with B1 symmetry, this calculation gives the following relations

$$\chi^{(2)}_{\text{psp}} = -\frac{1}{2}(\beta_{abc} - \beta_{bac})\cos^2[\phi] = 0 \tag{3}$$

$$\chi^{(2)}_{\text{spp}} = +\frac{1}{2}(\beta_{abc} - \beta_{bac})\cos^2[\phi] = 0 \tag{4}$$

$$\chi^{(2)}_{\text{ssp}} = 0 \tag{5}$$

$$\chi^{(2)}_{\text{ppp}} = 0 \tag{6}$$

From Table 2, we can see that $\beta_{\text{abc}} = \beta_{\text{bac}} = -0.039$. This gives $\chi^{(2)}_{\text{psp}} = \chi^{(2)}_{\text{spp}} = \chi^{(2)}_{\text{ssp}} = \chi^{(2)}_{\text{ppp}}$, explaining the absence of the 1698 cm^{-1} peak with B1 symmetry in the SFG spectra of the *B. mori* silk.

For the normal mode with B2 symmetry, the integration of all possible twist angles at $\theta = 90°$ using the $\beta_{i'j'k'}$ terms obtained by eq 2 gives the following nonlinear susceptibility equations for the four polarizations used in this experiment[38]

$$\chi^{(2)}_{\text{psp}} \cong 0.4\beta_{cab}(1 - 3\cos[2\phi]) \tag{7}$$

$$\chi^{(2)}_{\text{spp}} \cong 0.4\beta_{cab}(1 + \cos[2\phi]) \tag{8}$$

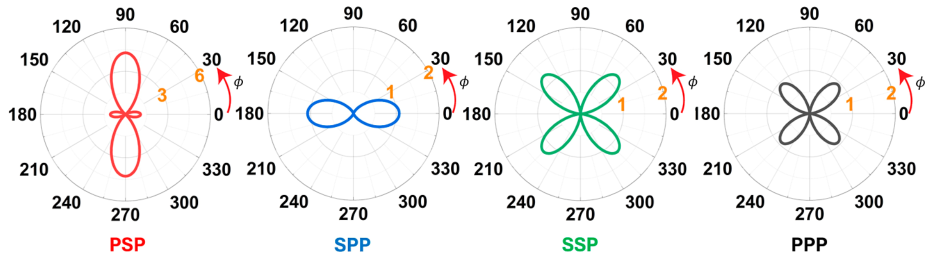

Figure 5. Polar plots of $|\chi_{\text{eff}}^{(2)}|^2$ as a function of the fiber orientation with respect to the laser incidence plane of the antiparallel β sheet for psp, spp, ssp, and ppp polarizations where yellow numbers indicate the calculated relative intensity.

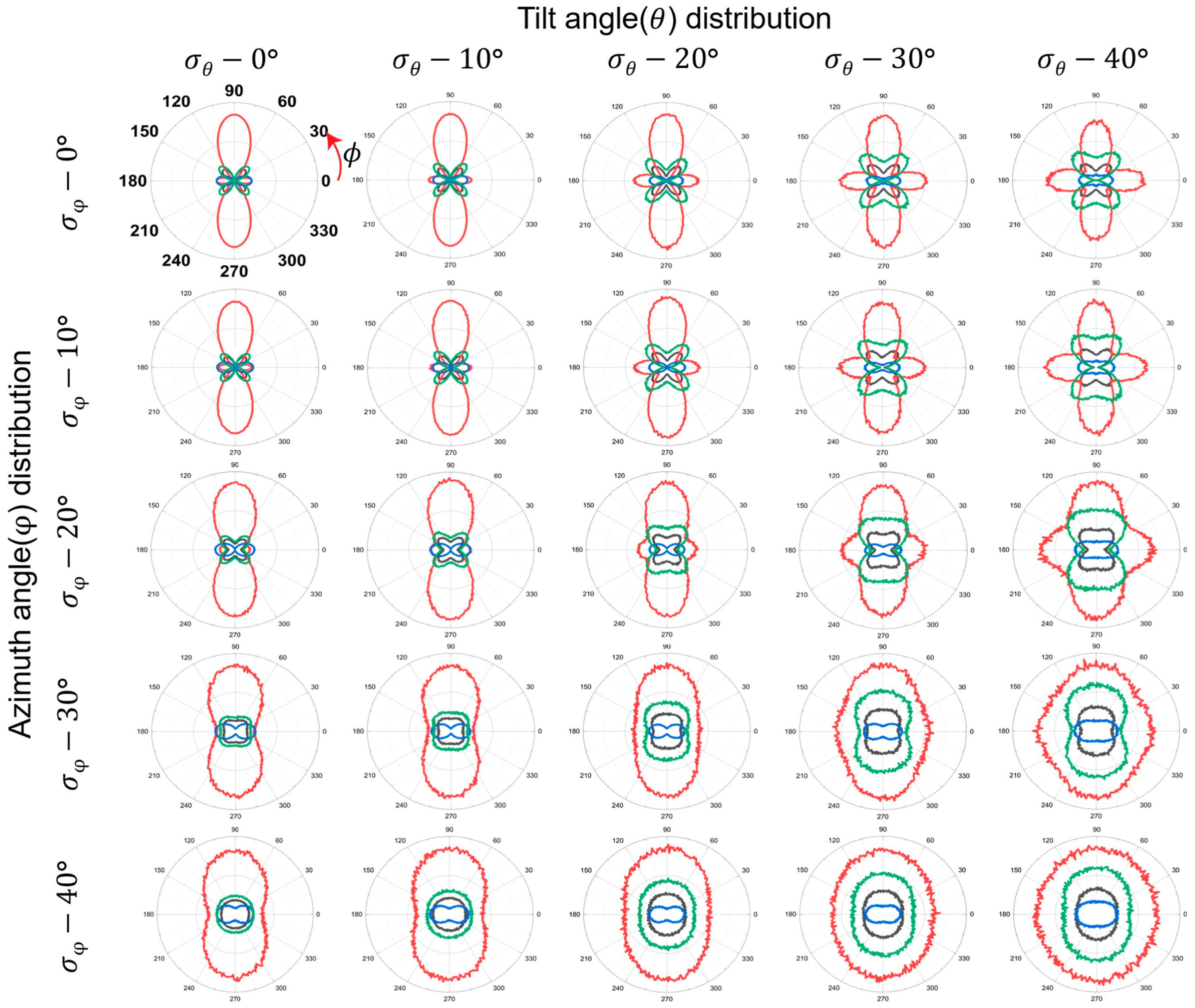

Figure 6. Simulated SFG polar plots of B2 mode, as a function of the fiber orientation with respect to the laser incident plane, for psp (red), spp (blue), ssp (green), and ppp (black) polarizations with different standard deviations of azimuth (σ_φ) and tilt (σ_θ) angles for the case with the average azimuth and tilt angles of 0 and 90°, respectively.

$$\chi_{\text{ssp}}^{(2)} \cong 1.6\beta_{cab}\cos[\phi]\sin[\phi] \tag{9}$$

$$\chi_{\text{ppp}}^{(2)} \cong 1.4\beta_{cab}\cos[\phi]\sin[\phi] \tag{10}$$

Figure 5 compares the polar plots of the azimuth angle dependence of $|\chi_{\text{eff}}^{(2)}|^2$ for the normal mode with the B2 symmetry. The psp polarization shows two large lobes centered at ϕ = 90° and 270° and two small lobes centered at ϕ = 0° and 180°. The psp intensity at ϕ = 90° is significantly larger than the intensities at the other polarizations. In contrast, the spp polarization shows only two lobes centered at ϕ = 0° and 180° with the maximum intensity slightly larger than that of psp at ϕ = 0° and 180°. These qualitatively agree

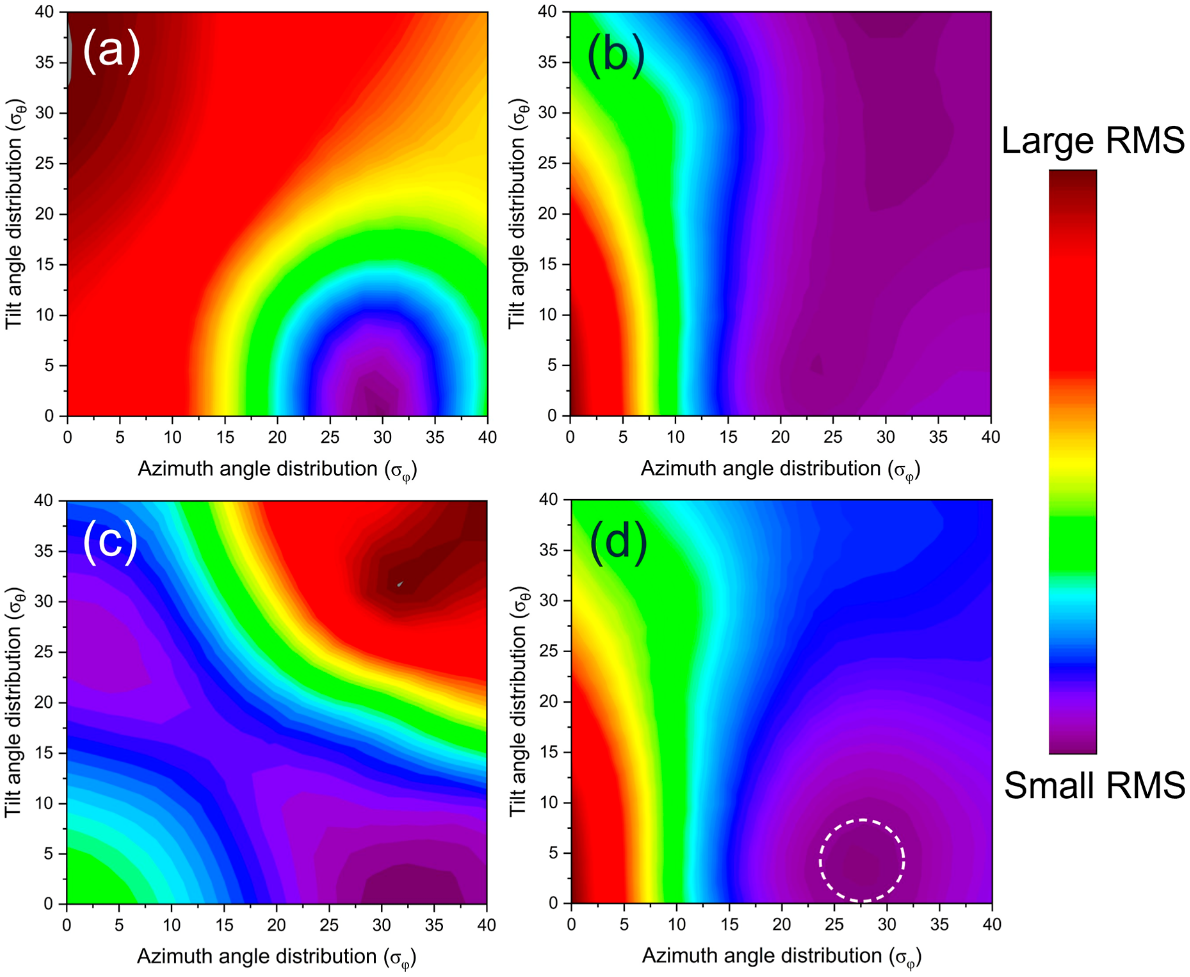

Figure 7. rmsd plot between the experiment and simulation result at (a) ϕ = 0°, (b) ϕ = 45°, and (c) ϕ = 90° and (d) for the sum of all three angles.

with the trends seen for the 1632 cm^{-1} peak in the psp and spp polarizations at ϕ = 0 and 90° in Figure 4a,e.

The normal mode with B3 symmetry shows the same pattern as the B2 mode with a much smaller intensity (see Figure S7). If the B3 mode intensity is calculated with the values in Table 2, it is about 8 times smaller than the B2 mode intensity. If the values proposed by Ye in Table S5 are used, the B3 intensity is predicted to be 3 times smaller than the B2 intensity. These relative intensity predictions are qualitatively consistent with the ratio of the 1667 and 1632 cm^{-1} intensities (Figures S3−S5). Based on this, we could tentatively assign that the 1667 cm^{-1} peak in the SFG spectra is the B3 mode.

The ssp and ppp polarizations are predicted to have four lobes centered at ϕ = 45, 135, 225, and 315°, and their intensities are expected to be larger than the psp and spp signals at those angles. This calculation result is not consistent with the data in Figure 4c. Note that the calculation result shown in Figure 5 is for the case in which both tilt angle (θ) and alignment angle (φ) distributions of the β-sheet domain are assumed to have a delta function. So, the discrepancy must be due to the ignorance of the orientation distribution.

To check the ϕ dependence of the psp-, spp-, ssp-, and ppp-SFG signals on the alignment and tilt angle distributions, we have numerically calculated the SFG peak intensity for the cases where the β-sheet domains are arranged with the Gaussian probability functions with different standard deviations in alignment (σ_φ) and tilt (σ_θ) angles, while keeping the φ = 0° and θ = 90°. The calculation was done with the algorithm published previously.[35] Figure 6 displays the ϕ-polar plots of the B2 mode obtained with σ_φ and σ_θ varying from 0 to 40° with a 10° increment. As σ_θ increases while keeping σ_φ constant, the difference in SFG intensity at ϕ = 0 and 90° decreases; in the meantime, the ssp and ppp intensities grow significantly. As σ_φ increases while keeping σ_θ constant, the ϕ dependence of the SFG signal becomes weaker in all four polarizations.

We can use the σ_φ and σ_θ dependences of the B2 mode as a reference data set and compare them with the experimental data to estimate the angular distribution of the crystalline β-sheet domains in the *B. mori* fiber. As mentioned before, the absolute intensities of the experimental data cannot be compared and only the relative intensities can be compared. For that reason, we took the spp/psp, ssp/psp, and ppp/psp ratios of the 1632 cm^{-1} SFG peak areas taken at ϕ = 0, 45, and 90° (Figure 4) and compared those ratios with the theoretically calculated intensity ratios of the B2 mode with different σ_φ and σ_θ distributions (Figure 6). Figure 7a,b,c plots the relative magnitude of the root-mean-square deviation (rmsd) between the experimental data and the theoretical calculations at ϕ = 0, 45, and 90°, respectively. Figure 7d shows the root-mean-square-deviation (rmsd) plot calculated with consideration of all three ϕ data together. These plots clearly show that the error is the largest if we assume that all β-sheet domains are perfectly aligned with $\varphi = 0^\circ$ and $\theta = 90^\circ$. The smallest error is found when $\sigma_\varphi \approx 27^\circ$ and $\sigma_\theta \approx 5^\circ$.

The angular distribution of $\sigma_\varphi \approx 27^\circ$ is in reasonably good agreement with the 2D-XRD analysis. The rocking curves of the (002) and (120) diffraction peaks extracted from Figure 1c are shown in Figures S8 and S9. The fwhm of the (002) and (120) diffraction peaks is 16 and 21°, respectively. This agreement demonstrates that SFG can be used to selectively analyze not only the vibrational modes of functional groups involved in interchain hydrogen bonds within the unit cell of the crystalline β-sheet domain (Figures 2 and 3) but also the angular distribution of the crystallites within *B. mori* silk fiber (Figures 4 and 7). The same methodology can be applied to other silk fibers, and the method itself could be improved further by combining with density functional theory calculations to obtain the full set of polarizability and dipole tensors of all amide modes, which are the subject of future study.

CONCLUSIONS

Vibrational SFG spectroscopy can be used for selective detection of amide I-, II-, III-, and -A bands originating from crystalline β-sheet domains in *B. mori* silk fiber. Based on the noncentrosymmetry selection rule, the SFG spectral features can be analyzed to obtain structural information on β-sheet domains, without suffering from interferences from amorphous protein portions in the sample. In this study, the amide-I band was primarily investigated by comparing SFG experimental observations and theoretical predictions simulated using the hyperpolarizability tensors based on the B2 symmetry of the D_2 point group. This analysis found that crystalline β-sheet domains are aligned along the fiber axis with a standard deviation of ~27° and parallel to the fiber surface with a standard deviation of ~5°. Although all SFG-active amide vibrational modes have not yet been fully deciphered, this approach can still be applied to the amide-I band analysis of β-sheet domains in other silk fibers. Thus, SFG analysis has a potential to find the structural information critically needed to unveil the structure−mechanical property relationship by characterizing hydrogen-bonding interactions at the nanoscale and alignments of β-sheet domains at the mesoscale.

ASSOCIATED CONTENT

Supporting Information

The Supporting Information is available free of charge at https://pubs.acs.org/doi/10.1021/acs.biomac.4c00774.

> Schematic orientation of the antiparallel β-sheet unit (a, b, c) in the laboratory coordinate system (X, Y, Z) as a function of azimuth angle (ϕ), tilt angle (θ), and twist angle (ψ); WAXS radial spectra of *B. mori* fibers for the equator and meridian; parameters of WAXS radial scanning spectra for *B. mori* fibers; deconvoluted SFG spectra at ϕ = 0, 45, and 90° for four polarization combinations (psp, spp, ssp, and ppp); comparison of normal mode symmetry in the D_2 point group of the antiparallel β sheet calculated by Nguyen et al. and Ye et al.; comparison of polar plots of the SFG intensity ($|\chi_{\mathrm{eff}}^{(2)}|^2$) between B2 and B3 symmetries for the antiparallel β sheet using tensors from Nguyen et al. and Ye et al., as a function of the fiber orientation with respect to the laser incidence plane; rocking curve profile of the (002) plane with a 2θ range from 25.0 to 26.0°; and rocking curve profile of the (120) plane with a 2θ range from 19.5 to 21.5° (PDF)

AUTHOR INFORMATION

Corresponding Author

Seong H. Kim − *Department of Chemical Engineering, Materials Research Institute, Pennsylvania State University, University Park, Pennsylvania 16802, United States*; orcid.org/0000-0002-8575-7269; Email: shk10@psu.edu

Authors

Jihyeong Ryu − *Department of Chemical Engineering, Materials Research Institute, Pennsylvania State University, University Park, Pennsylvania 16802, United States*; orcid.org/0009-0000-8797-9554

Juseok Choi − *Department of Chemical Engineering, Materials Research Institute, Pennsylvania State University, University Park, Pennsylvania 16802, United States*; orcid.org/0000-0002-0988-6544

Jongcheol Lee − *Department of Chemical Engineering, Materials Research Institute, Pennsylvania State University, University Park, Pennsylvania 16802, United States*; orcid.org/0000-0003-4877-901X

Complete contact information is available at: https://pubs.acs.org/10.1021/acs.biomac.4c00774

Notes

The authors declare no competing financial interest.

ACKNOWLEDGMENTS

This work was supported by the National Science Foundation (grant no. NSF-2203635).

REFERENCES

(1) Gosline, J. M.; Guerette, P.; Ortlepp, C.; Savage, K. The mechanical design of spider silks: from fibroin sequence to mechanical function. *J. Exp. Biol.* **1999**, *202* (23), 3295−3303.

(2) Tokareva, O.; Jacobsen, M.; Buehler, M.; Wong, J.; Kaplan, D. L. Structure−function−property−design interplay in biopolymers: Spider silk. *Acta Biomater.* **2014**, *10* (4), 1612−1626.

(3) Barreiro, D. L.; Yeo, J.; Tarakanova, A.; Martin-Martinez, F. J.; Buehler, M. J. Multiscale Modeling of Silk and Silk-Based Biomaterials—A Review. *Macromol. Biosci.* **2019**, *19* (3), 1800253.

(4) Li, G.; Li, Y.; Chen, G.; He, J.; Han, Y.; Wang, X.; Kaplan, D. L. Silk-based biomaterials in biomedical textiles and fiber-based implants. *Adv. Healthcare Mater.* **2015**, *4* (8), 1134−1151.

(5) Huang, W.; Ling, S.; Li, C.; Omenetto, F. G.; Kaplan, D. L. Silkworm silk-based materials and devices generated using bio-nanotechnology. *Chem. Soc. Rev.* **2018**, *47* (17), 6486−6504.

(6) Chen, X.; Hou, D.; Wang, L.; Zhang, Q.; Zou, J.; Sun, G. Antibacterial surgical silk sutures using a high-performance slow-release carrier coating system. *ACS Appl. Mater. Interfaces* **2015**, *7* (40), 22394−22403.

(7) Guo, C.; Zhang, J.; Wang, X.; Nguyen, A. T.; Liu, X. Y.; Kaplan, D. L. Comparative study of strain-dependent structural changes of silkworm silks: insight into the structural origin of strain-stiffening. *Small* **2017**, *13* (47), 1702266.

(8) Guo, C.; Zhang, J.; Jordan, J. S.; Wang, X.; Henning, R. W.; Yarger, J. L. Structural comparison of various silkworm silks: An insight into the structure−property relationship. *Biomacromolecules* **2018**, *19* (3), 906−917.

(9) Shao, Z.; Vollrath, F. Surprising strength of silkworm silk. *Nature* **2002**, *418* (6899), 741.

(10) Plaza, G. R.; Corsini, P.; Marsano, E.; Pérez-Rigueiro, J.; Biancotto, L.; Elices, M.; Riekel, C.; Agulló-Rueda, F.; Gallardo, E.; Calleja, J. M.; et al. Old silks endowed with new properties. *Macromolecules* **2009**, *42* (22), 8977−8982.

(11) Lefevre, T.; Paquet-Mercier, F.; Rioux-Dubé, J.; Pézolet, M. Structure of silk by raman spectromicroscopy: From the spinning glands to the fibers. *Biopolymers* **2012**, *97* (6), 322−336.

(12) Drummy, L. F.; Farmer, B.; Naik, R. R. Correlation of the β-sheet crystal size in silk fibers with the protein amino acid sequence. *Soft Matter* **2007**, *3* (7), 877−882.

(13) Zhou, C.-Z.; Confalonieri, F.; Medina, N.; Zivanovic, Y.; Esnault, C.; Yang, T.; Jacquet, M.; Janin, J.; Duguet, M.; Perasso, R. Fine organization of Bombyx mori fibroin heavy chain gene. *Nucleic Acids Res.* **2000**, *28* (12), 2413−2419.

(14) Paquet-Mercier, F.; Lefèvre, T.; Auger, M.; Pézolet, M. Evidence by infrared spectroscopy of the presence of two types of β-sheets in major ampullate spider silk and silkworm silk. *Soft Matter* **2013**, *9* (1), 208−215.

(15) Takahashi, Y.; Gehoh, M.; Yuzuriha, K. Structure refinement and diffuse streak scattering of silk (Bombyx mori). *Int. J. Biol. Macromol.* **1999**, *24* (2−3), 127−138.

(16) Marsh, R. E.; Corey, R. B.; Pauling, L. An investigation of the structure of silk fibroin. *Biochim. Biophys. Acta* **1955**, *16*, 1−34.

(17) Lotz, B.; Cesari, F. C. The chemical structure and the crystalline structures of Bombyx mori silk fibroin. *Biochimie* **1979**, *61* (2), 205−214.

(18) Asakura, T.; Ohata, T.; Kametani, S.; Okushita, K.; Yazawa, K.; Nishiyama, Y.; Nishimura, K.; Aoki, A.; Suzuki, F.; Kaji, H.; et al. Intermolecular packing in B. mori silk fibroin: multinuclear NMR study of the model peptide (Ala-Gly) 15 defines a heterogeneous antiparallel antipolar mode of assembly in the silk II form. *Macromolecules* **2015**, *48* (1), 28−36.

(19) Shen, Y.; Johnson, M. A.; Martin, D. C. Microstructural characterization of Bombyx mori silk fibers. *Macromolecules* **1998**, *31* (25), 8857−8864.

(20) Barnette, A. L.; Lee, C.; Bradley, L. C.; Schreiner, E. P.; Park, Y. B.; Shin, H.; Cosgrove, D. J.; Park, S.; Kim, S. H. Quantification of crystalline cellulose in lignocellulosic biomass using sum frequency generation (SFG) vibration spectroscopy and comparison with other analytical methods. *Carbohydr. Polym.* **2012**, *89* (3), 802−809.

(21) Rizzo, G.; Petrelli, V.; Sibillano, T.; De Caro, L.; Giangregorio, M. M.; Lo Presti, M.; Omenetto, F. G.; Giannini, C.; Mastrorilli, P.; Farinola, G. M. Raman, WAXS, and Solid-State NMR Characterizations of Regenerated Silk Fibroin Using Lanthanide Ions as Chaotropic Agents. *ACS Omega* **2023**, *8* (27), 24165−24175.

(22) Asakura, T.; Okonogi, M.; Horiguchi, K.; Aoki, A.; Saitô, H.; Knight, D. P.; Williamson, M. P. Two different packing arrangements of antiparallel polyalanine. *Angew. Chem.* **2012**, *124* (5), 1238−1241.

(23) Barth, A.; Zscherp, C. What vibrations tell about proteins. *Q. Rev. Biophys.* **2002**, *35* (4), 369−430.

(24) Moore, W. H.; Krimm, S. Vibrational analysis of peptides, polypeptides, and proteins. II. β-Poly (L-alanine) and β-poly (L-alanylglycine). *Biopolymers* **1976**, *15* (12), 2465−2483.

(25) Ye, S.; Li, H.; Yang, W.; Luo, Y. Accurate determination of interfacial protein secondary structure by combining interfacial-sensitive amide I and amide III spectral signals. *J. Am. Chem. Soc.* **2014**, *136* (4), 1206−1209.

(26) Hahn, S. Effective representation of amide III, II, I, and A modes on local vibrational modes: Analysis of ab initio quantum calculation results. *J. Chem. Phys.* **2016**, *145* (16), 164113.

(27) Lefèvre, T.; Rousseau, M.-E.; Pézolet, M. Protein secondary structure and orientation in silk as revealed by Raman spectromicroscopy. *Biophys. J.* **2007**, *92* (8), 2885−2895.

(28) Hu, X.; Kaplan, D.; Cebe, P. Determining beta-sheet crystallinity in fibrous proteins by thermal analysis and infrared spectroscopy. *Macromolecules* **2006**, *39* (18), 6161−6170.

(29) Badillo-Sanchez, D.; Chelazzi, D.; Giorgi, R.; Cincinelli, A.; Baglioni, P. Characterization of the secondary structure of degummed Bombyx mori silk in modern and historical samples. *Polym. Degrad. Stab.* **2018**, *157*, 53−62.

(30) Barnette, A. L.; Bradley, L. C.; Veres, B. D.; Schreiner, E. P.; Park, Y. B.; Park, J.; Park, S.; Kim, S. H. Selective detection of crystalline cellulose in plant cell walls with sum-frequency-generation (SFG) vibration spectroscopy. *Biomacromolecules* **2011**, *12* (7), 2434−2439.

(31) Ogawa, Y.; Lee, C. M.; Nishiyama, Y.; Kim, S. H. Absence of sum frequency generation in support of orthorhombic symmetry of α-chitin. *Macromolecules* **2016**, *49* (18), 7025−7031.

(32) Lee, C. M.; Kafle, K.; Park, Y. B.; Kim, S. H. Probing crystal structure and mesoscale assembly of cellulose microfibrils in plant cell walls, tunicate tests, and bacterial films using vibrational sum frequency generation (SFG) spectroscopy. *Phys. Chem. Chem. Phys.* **2014**, *16* (22), 10844−10853.

(33) Kong, L.; Lee, C.; Kim, S. H.; Ziegler, G. R. Characterization of starch polymorphic structures using vibrational sum frequency generation spectroscopy. *J. Phys. Chem. B* **2014**, *118* (7), 1775−1783.

(34) Han, Y.; Hsu, J.; Ge, N.-H.; Potma, E. O. Polarization-sensitive sum-frequency generation microscopy of collagen fibers. *J. Phys. Chem. B* **2015**, *119* (8), 3356−3365.

(35) Choi, J.; Lee, J.; Makarem, M.; Huang, S.; Kim, S. H. Numerical Simulation of Vibrational Sum Frequency Generation Intensity for Non-Centrosymmetric Domains Interspersed in an Amorphous Matrix: A Case Study for Cellulose in Plant Cell Wall. *J. Phys. Chem. B* **2022**, *126* (35), 6629−6641.

(36) Wang, H. F.; Gan, W.; Lu, R.; Rao, Y.; Wu, B. H. Quantitative spectral and orientational analysis in surface sum frequency generation vibrational spectroscopy (SFG-VS). *Int. Rev. Phys. Chem.* **2005**, *24* (2), 191−256.

(37) Choi, J.; Kwansa, A. L.; Yingling, Y. G.; Kim, S. H. DFT-Based Calculation of Molecular Hyperpolarizability and SFG Intensity of Symmetric and Asymmetric Stretch Modes of Alkyl Groups. *J. Phys. Chem. B* **2023**, *127* (39), 8456−8467.

(38) Nguyen, K. T.; King, J. T.; Chen, Z. Orientation Determination of Interfacial β-Sheet Structures in Situ. *J. Phys. Chem. B* **2010**, *114* (25), 8291−8300.

(39) Ye, S.; Wei, F.; Li, H.; Tian, K.; Luo, Y. Chapter Seven—Structure and orientation of interfacial proteins determined by sum frequency generation vibrational spectroscopy: method and application. *Adv. Protein Chem. Struct. Biol.* **2013**, *93*, 213−255.

(40) Rockwood, D. N.; Preda, R. C.; Yücel, T.; Wang, X.; Lovett, M. L.; Kaplan, D. L. Materials fabrication from Bombyx mori silk fibroin. *Nat. Protoc.* **2011**, *6* (10), 1612−1631.

(41) Lee, C. M.; Kafle, K.; Huang, S.; Kim, S. H. Multimodal broadband vibrational sum frequency generation (MM-BB-V-SFG) spectrometer and microscope. *J. Phys. Chem. B* **2016**, *120* (1), 102−116.

(42) Tsukada, M.; Nagura, M.; Ishikawa, H.; Shiozaki, H. Structural characteristics of silk fibers treated with epoxides. *J. Appl. Polym. Sci.* **1991**, *43* (4), 643−649.

(43) Boulet-Audet, M.; Terry, A. E.; Vollrath, F.; Holland, C. Silk protein aggregation kinetics revealed by Rheo-IR. *Acta Biomater.* **2014**, *10* (2), 776−784.

(44) Makarem, M.; Lee, C. M.; Kafle, K.; Huang, S.; Chae, I.; Yang, H.; Kubicki, J. D.; Kim, S. H. Probing cellulose structures with vibrational spectroscopy. *Cellulose* **2019**, *26*, 35−79.

(45) Ngo, D.; Liu, H.; Chen, Z.; Kaya, H.; Zimudzi, T. J.; Gin, S.; Mahadevan, T.; Du, J.; Kim, S. H. Hydrogen bonding interactions of H2O and SiOH on a boroaluminosilicate glass corroded in aqueous solution. *npj Mater. Degrad.* **2020**, *4* (1), 1.

(46) Ling, S.; Qi, Z.; Knight, D. P.; Shao, Z.; Chen, X. Synchrotron FTIR microspectroscopy of single natural silk fibers. *Biomacromolecules* **2011**, *12* (9), 3344−3349.

(47) Yan, E. C.; Wang, Z.; Fu, L. Proteins at interfaces probed by chiral vibrational sum frequency generation spectroscopy. *J. Phys. Chem. B* **2015**, *119* (7), 2769−2785.

(48) Hu, X.; Lu, Q.; Kaplan, D. L.; Cebe, P. Microphase Separation Controlled β-Sheet Crystallization Kinetics in Fibrous Proteins. *Macromolecules* **2009**, *42* (6), 2079−2087.

(49) Ha, S.-W.; Tonelli, A. E.; Hudson, S. M. Structural studies of bombyx m ori silk fibroin during regeneration from solutions and wet fiber spinning. *Biomacromolecules* **2005**, *6* (3), 1722−1731.

(50) Makarem, M.; Lee, C. M.; Sawada, D.; O'Neill, H. M.; Kim, S. H. Distinguishing surface versus bulk hydroxyl groups of cellulose nanocrystals using vibrational sum frequency generation spectroscopy. *J. Phys. Chem. Lett.* **2018**, *9* (1), 70−75.

(51) Lee, C. M.; Mittal, A.; Barnette, A. L.; Kafle, K.; Park, Y. B.; Shin, H.; Johnson, D. K.; Park, S.; Kim, S. H. Cellulose polymorphism study with sum-frequency-generation (SFG) vibration spectroscopy: identification of exocyclic CH_2OH conformation and chain orientation. *Cellulose* **2013**, *20*, 991−1000.

(52) Wu, F.-C.; Tseng, R.-L.; Juang, R.-S. Initial behavior of intraparticle diffusion model used in the description of adsorption kinetics. *Chem. Eng. J.* **2009**, *153* (1−3), 1−8.

(53) Schwaab, M.; Steffani, E.; Barbosa-Coutinho, E.; Júnior, J. B. S. Critical analysis of adsorption/diffusion modelling as a function of time square root. *Chem. Eng. Sci.* **2017**, *173*, 179−186.

(54) Chen, X.; Shao, Z.; Marinkovic, N. S.; Miller, L. M.; Zhou, P.; Chance, M. R. Conformation transition kinetics of regenerated Bombyx mori silk fibroin membrane monitored by time-resolved FTIR spectroscopy. *Biophys. Chem.* **2001**, *89* (1), 25−34.

(55) Zhong, J.; Liu, Y.; Ren, J.; Tang, Y.; Qi, Z.; Zhou, X.; Chen, X.; Shao, Z.; Chen, M.; Kaplan, D. L.; et al. Understanding secondary structures of silk materials via micro-and nano-infrared spectroscopies. *ACS Biomater. Sci. Eng.* **2019**, *5* (7), 3161−3183.

(56) Miyazawa, T.; Blout, E. The infrared spectra of polypeptides in various conformations: Amide I and II bands1. *J. Am. Chem. Soc.* **1961**, *83* (3), 712−719.

(57) Lefèvre, T.; Paquet-Mercier, F.; Lesage, S.; Rousseau, M.-E.; Bédard, S.; Pézolet, M. Study by Raman spectromicroscopy of the effect of tensile deformation on the molecular structure of Bombyx mori silk. *Vib. Spectrosc.* **2009**, *51* (1), 136−141.

(58) Even, M. A.; Lee, S.-H.; Wang, J.; Chen, Z. Detection and spectral analysis of trifluoromethyl groups at a surface by sum frequency generation vibrational spectroscopy. *J. Phys. Chem. B* **2006**, *110* (51), 26089−26097.

(59) Marsh, D. Dichroic ratios in polarized Fourier transform infrared for nonaxial symmetry of beta-sheet structures. *Biophys. J.* **1997**, *72* (6), 2710−2718.

(60) Yan, E. C.; Fu, L.; Wang, Z.; Liu, W. Biological macromolecules at interfaces probed by chiral vibrational sum frequency generation spectroscopy. *Chem. Rev.* **2014**, *114* (17), 8471−8498.

(61) Barth, A. Infrared spectroscopy of proteins. *Biochim. Biophys. Acta, Bioenerg.* **2007**, *1767* (9), 1073−1101.